

Channel Uncertainty-Aware Robust Beamforming for RIS-Assisted RSMA Communication With Movable Antennas

Muhammad Asif , Asim Ihsan , Zhongliang Wang , Manzoor Ahmed , *Member, IEEE*, Xingwang Li , *Senior Member, IEEE*, Arumugam Nallanathan , *Fellow, IEEE*, and Symeon Chatzinotas , *Fellow, IEEE*

Abstract—This work investigates a robust resource allocation framework for a downlink multi-user communication system integrating movable antennas (MAs) and reconfigurable intelligent surfaces (RISs) under the rate-splitting multiple access (RSMA) transmission protocol. Unlike conventional fixed-position antenna architectures, the considered MAs-enabled system introduces spatially adaptive channel variations in which antenna positions directly influence the effective channel responses. Consequently, under imperfect channel state information (CSI), the impact of CSI uncertainty propagates not only through active and passive beamforming design, but also through the antenna position optimization process, leading to a highly coupled robust optimization problem. To address this challenge, we formulate a system sum-rate maximization problem by jointly optimizing the transmit precoding vectors, RIS reflection matrix, common-rate allocation, and MAs positions, subject to quality-of-service (QoS), power-budget, common-rate decoding, and mutual coupling constraints. The resulting non-convex problem is efficiently handled through an iterative robust optimization framework, where the original problem is successively decomposed into active beamforming, RIS reflection matrix, and MAs position optimization subproblems, and tractable convex surrogate functions are constructed to enable iterative optimization. Moreover, system robustness is ensured by incorporating a bounded CSI uncertainty model that explicitly captures channel estimation errors and guarantees reliable communication performance under worst-case channel conditions. Finally, extensive simulation results demonstrate that the proposed framework achieves significant performance gains and enhanced robustness compared with benchmark schemes, while also exhibiting fast and stable convergence behavior under practical imperfect CSI conditions.

Index Terms—Movable antennas (MAs), reconfigurable intelligent surface (RIS), rate-splitting multiple access (RSMA), robust beamforming, channel uncertainty.

I. INTRODUCTION

This work was supported in part by the Natural Science Research Project of Anhui Educational Committee (2023AH040232, KJ2016A884-2025).

Muhammad Asif is with the School of Electrical Engineering, Tongling University, Anhui, Tongling, China (e-mail: masif@tlu.edu.cn).

Asim Ihsan is with the Interdisciplinary Research Center for Communication Systems and Sensing, King Fahd University of Petroleum & Minerals (KFUPM) Dhahran, Saudi Arabia (e-mail: asim.ihsan@kfupm.edu.sa).

Zhongliang Wang with the School of Electrical Engineering, Tongling University, Anhui, Tongling, China, and also with the Engineering Technology Research Center of Optoelectronic Technology Appliance, Anhui Province, Tongling, China (e-mail: asdwzl@tlu.edu.cn).

Manzoor Ahmed is with the School of Computer and Information Science and the Institute for AI Industrial Technology Research, Hubei Engineering University, Xiaogan 432000, China (e-mail: manzoor.achakzai@gmail.com).

Xingwang Li is with the School of Physics and Electronic Information Engineering, Henan Polytechnic University, Jiaozuo, 454003, China (e-mail: lixingwangbupt@gmail.com).

Arumugam Nallanathan is with the School of Electronic Engineering and Computer Science, Queen Mary University of London, E1 4NS London, U.K. (email: a.nallanathan@qmul.ac.uk).

Symeon Chatzinotas is with the Interdisciplinary Centre for Security, Reliability and Trust (SnT), University of Luxembourg, 1855 Luxembourg City, Luxembourg (e-mail: symeon.chatzinotas@uni.lu).

THE rapid evolution of wireless communication systems has fueled growing interest in the development of sixth-generation (6G) networks [1], [2]. The future 6G communication systems are likely to offer new performance requirements such as high data rates, high reliability, and better spectral efficiency, which will require new transmission technologies to be explored [3]–[5]. In this context, Multi-antenna communication technologies, especially multiple-input multiple-output (MIMO) systems, are among the most promising schemes that have been extensively analyzed due to their ability to exploit spatial multiplexing for improving both spectral and energy efficiency [6], [7]. Moreover, in future wireless networks, the growing adoption of high-frequency bands with shorter signal wavelengths facilitates the practical implementation of large antenna arrays and enables massive MIMO systems to achieve substantial beamforming and spatial multiplexing gains [8]–[10].

However, the traditional MIMO architectures rely on antennas deployed at fixed locations, which fundamentally limits the spatial degrees of freedom available for diversity and multiplexing gains. Recently, a new frontier technology known as movable antennas (MAs) has been introduced, providing a novel paradigm in which antennas can dynamically adjust their positions within a small region to fully exploit spatial degrees of freedom, resulting in improved communication performance [11], [12]. Specifically, in MAs-assisted systems, each antenna element is connected to its corresponding radio frequency (RF) chain through a flexible cable, allowing it to move freely within a predefined spatial region, thereby enabling more favorable channel conditions and improved system performance. In addition, MAs-enables systems can effectively mitigate multiuser interference by repositioning themselves from locations with strong interference to positions where interference is weaker. By independently adjusting the locations of different MAs, the spatial adjustment of antennas enables a more effective exploitation of spatial degrees of freedom, thereby improving diversity and multiplexing performance. In this context, recent studies have demonstrated that MAs-assisted systems achieve superior communication performance compared to fixed-position antennas (FPA)-based systems. Authors in [12] introduced the concept of MAs and established a far-field channel model based on the field-response formulation. Using this model, they analyzed the maximum achievable channel gain of MAs-assisted systems with a single movable antenna deployed at both the transmitter and receiver nodes. Their results demonstrated that MAs systems can significantly outperform FPA counterparts, especially in rich multipath environments. In [13], the authors investigated MAs-assisted multiuser uplink communications by proposing a base station architecture equipped with multiple movable antennas. They

formulated a max–min rate optimization problem by jointly optimizing the antenna positions, receive combining, and users’ transmit powers under practical constraints. Likewise, the work in [14] investigated beamforming with movable antenna arrays to overcome the inherent trade-off between array gain and interference suppression in FPA systems. By jointly optimizing the antenna position vector and antenna weight vector, it is demonstrated that full array gain toward the desired direction and null steering toward multiple interference directions can be simultaneously achieved. Further, Ma *et al.* in [15] investigated a MAs-enabled point-to-point MIMO systems for capacity enhancement through antenna position optimization. By jointly optimizing the positions of MAs and transmit beamforming, the authors characterized the capacity gains achievable with MAs over FPA systems. Further, authors in [16] investigated a MAs-enabled wide-band communication system by considering OFDM transmission over frequency-selective fading channels. A multi-tap field-response channel model is employed to characterize the joint spatial–frequency channel variations induced by antenna movement.

Recently, rate-splitting multiple access (RSMA) has been widely investigated as a non-orthogonal physical-layer transmission paradigm, due to its superior spectral efficiency and enhanced ability to manage interference [17]. RSMA operates by splitting each user’s message into common and private components, which enables partial decoding of multiuser interference while treating the remaining interference as noise. Through proper message splitting and power control between the common and private messages, RSMA is able to dynamically support a broad spectrum of interference management strategies ranging from complete interference treatment as noise to complete interference decoding [18]. Owing to this natural flexibility, RSMA is able to fill the existing gap between space-division multiple access (SDMA), which is based on treating interference as noise, and non-orthogonal multiple access (NOMA), which focuses on decoding dominant interference signals. Thus, the balanced transmission system of RSMA supports enhanced spectral and energy efficiency [19], while also providing increased robustness in multiuser communication environments characterized by adverse operating conditions.

Despite RSMA offers superior spectral efficiency and interference mitigation capabilities, blockage of the direct communication link can substantially impair its performance, giving rise to coverage holes and increased outage probability. To overcome this limitation, reconfigurable intelligent surface (RIS) has emerged as an effective solution that enhances capacity, reliability, and coverage by dynamically shaping the wireless propagation environment [20]. An RIS typically consists of a planar array composed of a large number of passive reflecting elements. By adaptively adjusting the reflection coefficients of these elements, the RIS can intelligently manipulate the wireless propagation environment [21]. In particular, through optimized reflection control, the RIS is able to steer incident signals toward intended users, thereby reshaping the channel conditions and alleviating coverage blind spots [22], [23]. As a result, due to its largely passive operation, with power consumption mainly associated with the control

circuitry, RIS offers a cost-effective, low-maintenance, and easily deployable solution.

Inspired by the aforementioned advantages, the deployment of MAs in conjunction with RSMA transmission and RIS-assisted propagation control is expected to offer a promising approach for achieving adaptive spatial control, high spectral efficiency, and reliable coverage in future 6G systems. In this regard, authors in [24] investigated a downlink coordinated multi-point RSMA system in which users are equipped with MAs to exploit spatial adaptability. A joint optimization framework was considered to maximize the system sum-rate by optimizing base-station (BS) beamforming, common stream allocation, and MAs positions under quality-of-service (QoS) constraints. Further, Li *et al.* studied a MAs-assisted RSMA framework for short-packet ultra-reliable and low-latency communication transmission. A joint beamforming and antenna position optimization problem was formulated to maximize the achievable sum rate while satisfying stringent latency and reliability requirements [25]. In [26], authors investigated a MAs-aided uplink RSMA framework for supporting mobile broadband reliable low-latency communication under short-packet transmission. A sum-rate maximization problem was formulated by jointly optimizing antenna positions, receive combining, power allocation, and SIC decoding order. Likewise, the work in [27] studied a MAs-aided RIS-assisted integrated sensing and communication (ISAC) system to enhance communication and sensing performance in coverage-limited regions. A max–min beam-pattern gain optimization problem was considered by jointly optimizing the BS covariance matrix, RIS reflection coefficients, and MAs positions under practical constraints. Ma *et al.* in [28] investigated a MAs-assisted RIS-enabled ISAC system with a focus on enhancing physical-layer security against eavesdropping. A sum-rate maximization problem was formulated by jointly optimizing BS beamforming, RIS reflection coefficients, and MA positions. The authors in [29] considered an RIS-aided multiuser communication system enhanced by MAs to improve channel capacity. A joint optimization problem was formulated to characterize system performance by optimizing the RIS reflection coefficients, MA positions, and BS beamforming, and an efficient fractional programming–based algorithm was proposed to solve the resulting non-convex problem. In [30], covert rate maximization problem was investigated by jointly optimizing MAs movement trajectories, transmit beamforming, and RIS phase shifts. Moreover, authors in [31] studied a simultaneously transmitting and reflecting RIS-aided multiuser communication system enhanced by MAs to improve sum-rate performance under statistical channel-state information (CSI). A joint optimization problem was formulated to optimize STAR-RIS transmission and reflection coefficients, BS beamforming, and MA positions.

It is worth noting that the studies in [24]–[26] have proposed various optimization strategies for MAs-assisted RSMA networks. In addition, the works in [27]–[31] have developed several optimization frameworks for MAs-enabled RIS-empowered networks. Nevertheless, robust resource allocation frameworks for RIS-empowered MAs-enabled RSMA systems under practical CSI uncertainty conditions remain largely un-

explored. To the best of our knowledge, the only existing work investigating RIS-empowered MAs-enabled RSMA systems is reported in [32], where the optimization framework is developed under the assumption of perfect CSI. However, in MAs-enabled systems, antenna positions directly influence the effective channel responses, causing CSI uncertainty to propagate not only through the active and passive beamforming design, but also through the antenna position optimization process. Consequently, the resulting robust resource allocation problem becomes significantly more coupled and challenging compared with conventional RIS-assisted RSMA systems employing fixed-position antennas. Motivated by these limitations, we develop a robust resource allocation framework for RIS-empowered MAs-assisted multi-user RSMA systems that explicitly accounts for bounded CSI uncertainty while jointly optimizing active beamforming, RIS reflection matrix, common-rate allocation, and MAs positions under QoS requirements of users. In particular, the proposed framework captures the coupled impact of CSI uncertainty on both wireless propagation control and spatial antenna adaptation, thereby enhancing communication robustness in dynamic wireless environments. Moreover, by jointly exploiting the spatial flexibility of movable antennas, the passive beamforming capability of RIS, and the interference management benefits of RSMA, the proposed design provides an effective approach for improving spectral efficiency and system robustness under practical imperfect CSI conditions.

The key contributions are outlined as follows:

- We develop a robust resource allocation framework for RIS-empowered MAs-assisted multi-user downlink RSMA systems under bounded CSI uncertainty. Unlike conventional fixed-position antenna architectures, the considered MAs-enabled system introduces MAs-dependent channel responses and spatially coupled CSI uncertainty, where channel uncertainty propagates not only through active and passive beamforming design, but also through the antenna position optimization process, resulting in a highly coupled robust optimization problem.
- To address the resulting non-convex coupled optimization problem, we develop an efficient iterative robust optimization framework that jointly optimizes active beamforming, RIS reflection matrix, common-rate allocation, and MAs positions under QoS constraints. Specifically, the original problem is successively decomposed into active beamforming, RIS reflection matrix, and MAs position optimization subproblems, where tractable convex surrogate functions are constructed for the highly coupled non-convex objective and constraints, thereby enabling efficient iterative optimization under practical imperfect CSI conditions.
- Furthermore, the proposed framework explicitly captures the coupled impact of CSI uncertainty on wireless propagation control and spatial antenna adaptation by incorporating a bounded channel uncertainty model into the joint optimization process. In particular, the proposed design reveals how spatial antenna adaptation can be jointly leveraged with RIS-assisted propagation control to

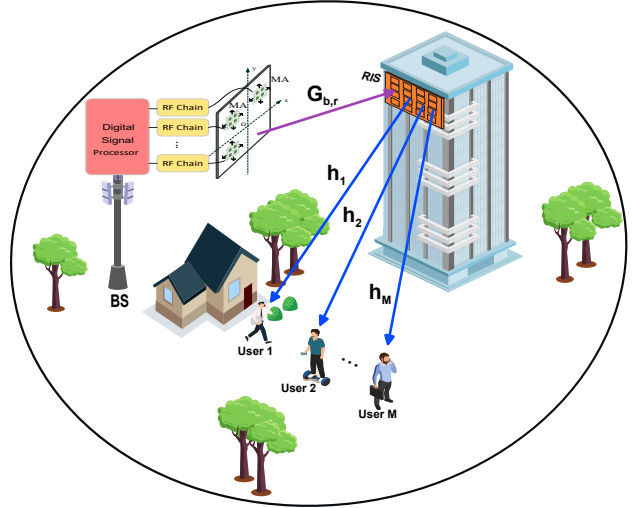


Fig. 1: Illustration of system model.

improve communication robustness and reliability under practical CSI uncertainty conditions.

- Finally, extensive simulation results demonstrate that jointly exploiting the spatial flexibility of movable antennas, the passive beamforming capability of RIS, and the interference management benefits of RSMA provides substantial gains in spectral efficiency and robustness compared with benchmark schemes, while also exhibiting fast and stable convergence behavior.

II. SYSTEM MODEL AND OPTIMIZATION PROBLEM FORMULATION

As depicted in Fig. 1, we consider a downlink system where a BS equipped with L MAs serves M single-antenna RSMA users under channel estimation errors. In the presence of environmental obstructions, the direct BS–user communication links are blocked, such that user transmission is realized exclusively through the RIS equipped with N reflecting elements.

A. Channel Model

In this work, we adopt a planar far-field response channel model [12], where the spatial extent of the MA transmit region is sufficiently small relative to the propagation distance between the transmitter and the receiver. Specifically, under planar far-field response model, the transmit/receive path of same channel experiences same angle-of-departure (AoD), angle-of-arrival (AoA), and amplitude of path response coefficient, whereas the phase of each path response coefficient varies across different MAs positions due to their distinct spatial locations.

Next, let us define the positions of L MAs as $\hat{\mathbf{t}} = [\hat{\mathbf{t}}_1, \hat{\mathbf{t}}_2, \dots, \hat{\mathbf{t}}_L] \in \mathbb{R}^{2 \times L}$, where $\hat{\mathbf{t}}_l = [x_l, y_l]^T \in \mathcal{C}_t$ denotes the position of l -th MA, $\forall l \in \mathcal{L} = \{1, 2, \dots, L\}$, \mathcal{C}_t denotes the transmit region of L MAs at BS. Further, let L_t and L_r denote the numbers of transmit and receive paths, respectively. The elevation and azimuth angles at the BS and the RIS are denoted by $\phi_i^e \in [0, \pi]$ and $\phi_i^a \in [0, \pi]$, for $1 \leq i \leq L_t$,

and $\varphi_j^e \in [0, \pi]$ and $\varphi_j^a \in [0, \pi]$, for $1 \leq j \leq L_r$, respectively. Then, the difference of the signal propagation distance for i -th transmit path between $\hat{\mathbf{t}}_i$ and reference origin is given as

$$\chi(\hat{\mathbf{t}}_i, \phi_i^e, \phi_i^a) = x_i \sin \phi_i^e \cos \phi_i^a + y_i \cos \phi_i^e. \quad (1)$$

Then, for BS-RIS link, the field response vector (FRV) of MA at $\hat{\mathbf{t}}_i$ is given as

$$\mathbf{f}^t(\hat{\mathbf{t}}_i) = \left[e^{j\frac{2\pi}{\lambda}\chi(\hat{\mathbf{t}}_i, \phi_i^e, \phi_i^a)}, \dots, e^{j\frac{2\pi}{\lambda}\chi(\hat{\mathbf{t}}_i, \phi_{L_i}^e, \phi_{L_i}^a)} \right]^T \in \mathbb{C}^{L_t \times 1}, \quad (2)$$

where $2\pi\chi(\hat{\mathbf{t}}_i, \phi_i^e, \phi_i^a)/\lambda$, for $1 \leq i \leq L_t$, denotes the phase difference of the i -th transmit path between the MA position $\hat{\mathbf{t}}_i$ and the reference origin, and λ represents the carrier wavelength. Accordingly, the field response matrix (FRM) for BS-RIS communication link for all L MAs is given as

$$\mathbf{F}^t(\hat{\mathbf{t}}) \triangleq \left[\mathbf{f}^t(\hat{\mathbf{t}}_1), \mathbf{f}^t(\hat{\mathbf{t}}_2), \dots, \mathbf{f}^t(\hat{\mathbf{t}}_L) \right] \in \mathbb{C}^{L_t \times L}. \quad (3)$$

Similarly, the FRV of n -th reflecting element of RIS at position $\hat{\mathbf{r}}_n = [x_n, y_n]^T$ is given by

$$\mathbf{f}^r(\hat{\mathbf{r}}_n) = \left[e^{j\frac{2\pi}{\lambda}\chi(\hat{\mathbf{r}}_n, \varphi_1^e, \varphi_1^a)}, \dots, e^{j\frac{2\pi}{\lambda}\chi(\hat{\mathbf{r}}_n, \varphi_{L_r}^e, \varphi_{L_r}^a)} \right]^T \in \mathbb{C}^{L_r \times 1}, \quad (4)$$

where $2\pi\chi(\hat{\mathbf{r}}_n, \varphi_j^e, \varphi_j^a)/\lambda$, for $1 \leq j \leq L_r$, denotes the phase difference of the j -th receive path between the position $\hat{\mathbf{r}}_n$ and reference origin of the RIS node. Accordingly, the FRM at RIS can be given as

$$\mathbf{F}^r(\hat{\mathbf{r}}) \triangleq \left[\mathbf{f}^r(\hat{\mathbf{r}}_1), \mathbf{f}^r(\hat{\mathbf{r}}_2), \dots, \mathbf{f}^r(\hat{\mathbf{r}}_N) \right] \in \mathbb{C}^{L_r \times N}. \quad (5)$$

Next, let $\mathbf{\Lambda} \in \mathbb{C}^{L_r \times L_t}$ denotes the path response matrix for BS-RIS link, then the equivalent channel from BS to the RIS can be written as

$$\mathbf{H}_{b,r}(\hat{\mathbf{t}}) = \mathbf{F}^r(\hat{\mathbf{r}})^H \mathbf{\Lambda} \mathbf{F}^t(\hat{\mathbf{t}}) \in \mathbb{C}^{N \times L}, \quad (6)$$

Next, let the channel from the RIS to the m -th user be denoted by $\mathbf{h}_{r,m} \in \mathbb{C}^{N \times 1}$. The resulting end-to-end equivalent channel from the BS to the m -th user can then be expressed as

$$\mathbf{g}_m^H(\hat{\mathbf{t}}) = \mathbf{h}_{r,m}^H \mathbf{\Phi} \mathbf{H}_{b,r}(\hat{\mathbf{t}}) \in \mathbb{C}^{1 \times L}, \quad (7)$$

where $\mathbf{\Phi} = \text{diag} \{ [e^{j\vartheta_1}, e^{j\vartheta_2}, \dots, e^{j\vartheta_N}]^T \} \in \mathbb{C}^{N \times N}$ denotes the reflection matrix of RIS.

B. Signal Model

Based on the RSMA transmission protocol, each user's message is split into a private part and a common part. Specifically, the private messages of the M users are independently encoded into M private data streams, denoted by $\{\hat{z}_1, \hat{z}_2, \dots, \hat{z}_M\}$, where $m \in \mathcal{M} = \{1, 2, \dots, M\}$, while the common messages intended for all users are jointly encoded into a single common data stream, denoted by \hat{z}_c . Accordingly, the transmitted signal at the BS is given by

$$\mathbf{x} = \mathbf{p}_c \hat{z}_c + \sum_{m=1}^M \mathbf{p}_m \hat{z}_m, \quad \forall m \in \mathcal{M}, \quad (8)$$

where $\mathbf{p}_m \in \mathbb{C}^{L \times 1}$ and $\mathbf{p}_c \in \mathbb{C}^{L \times 1}$ denote the transmit beamforming vectors for the private and common data streams,

respectively. Further, assuming $\mathbb{E}[\|\hat{z}_m\|^2] = 1$ and $\mathbb{E}[\|\hat{z}_c\|^2] = 1$, $\forall m \in \mathcal{M}$, the signal received at the m -th user can be written as

$$\hat{y}_m = \mathbf{g}_m^H(\hat{\mathbf{t}}) \mathbf{x} + \hat{n}_m, \quad \forall m \in \mathcal{M}, \quad (9)$$

where $\hat{n}_m \sim \mathcal{CN}(0, \sigma_m^2)$ denotes the additive white Gaussian noise (AWGN) at the m -th user.

Further, to characterize the impact of channel uncertainty, the effective channel of the m -th user is modeled as $\hat{\mathbf{g}}_m = \mathbf{g}_m + \Delta \mathbf{g}_m$ [33], [34], where \mathbf{g}_m denotes the available channel estimate and $\Delta \mathbf{g}_m$ represents the corresponding estimation error, which is assumed to follow a circularly symmetric complex Gaussian distribution. The channel uncertainty is further bounded by $\|\Delta \mathbf{g}_m\| \leq \hat{\varrho}_m$ [34].

Thus, the achievable rate for decoding the common stream at the m -th user is given by

$$R_m^c = \log_2(1 + \Gamma_m^c), \quad \forall m \in \mathcal{M}, \quad (10)$$

where Γ_m^c denotes the signal-to-interference-plus-noise ratio (SINR), which is given as

$$\Gamma_m^c = \frac{|\hat{\mathbf{g}}_m^H \mathbf{p}_c|^2}{\sum_{i=1}^M |\hat{\mathbf{g}}_m^H \mathbf{p}_i|^2 + \hat{\sigma}_m^2}, \quad \forall m \in \mathcal{M}. \quad (11)$$

Once the common stream has been successfully decoded, its effect is eliminated from the received signal via successive interference cancellation (SIC) [17]. The receiver then proceeds to decode its intended private data stream, while treating the private streams intended for other users as residual interference. Accordingly, the achievable rate associated with the private message for the m -th user can be expressed as

$$R_m^p = \log_2(1 + \Gamma_m^p), \quad \forall m \in \mathcal{M}, \quad (12)$$

where Γ_m^p represents the SINR, which is given by

$$\Gamma_m^p = \frac{|\hat{\mathbf{g}}_m^H \mathbf{p}_m|^2}{\sum_{\substack{i=1 \\ i \neq m}}^M |\hat{\mathbf{g}}_m^H \mathbf{p}_i|^2 + \hat{\sigma}_m^2}, \quad \forall m \in \mathcal{M}. \quad (13)$$

Accordingly, the sum-rate of the considered system can be written as

$$\hat{R} = \sum_{m \in \mathcal{M}} \left(\hat{r}_m^c + R_m^p \right), \quad \forall m \in \mathcal{M}, \quad (14)$$

where \hat{r}_m^c denotes the actual common rate allocated to m -th user.

C. Problem Formulation

This work focuses on maximizing the sum-rate of a MAS-enabled RSMA-based RIS system by jointly optimizing the transmit precoding vectors \mathbf{p}_m and \mathbf{p}_c , the RIS reflection matrix $\mathbf{\Phi}$, and positions of the MAs $\hat{\mathbf{t}}$, subject to QoS requirements under a bounded CSI error model. Accordingly,

the resulting optimization problem is formulated as

$$\text{(P1)} \quad \max_{(\hat{r}_m^c, \mathbf{p}_c, \mathbf{p}_m, \Phi, \hat{\mathbf{t}})} \sum_{m=1}^M (\hat{r}_m^c + R_m^p), \quad (15a)$$

$$\text{s.t. } C_1: \hat{r}_m^c + R_m^p \geq R_{\min}, \|\Delta \mathbf{g}_m\| \leq \hat{\varrho}_m, \forall m \in \mathcal{M}, \quad (15b)$$

$$C_2: \sum_{m=1}^M \hat{r}_m^c \leq R_m^c, \|\Delta \mathbf{g}_m\| \leq \hat{\varrho}_m, \forall m \in \mathcal{M}, \quad (15c)$$

$$C_3: \|\mathbf{p}_c\|^2 + \sum_{m=1}^M \|\mathbf{p}_m\|^2 \leq P_t, \forall m \in \mathcal{M} \quad (15d)$$

$$C_4: |e^{j\vartheta_i}| = 1, \forall i \in \mathcal{N} = \{1, 2, \dots, N\}, \quad (15e)$$

$$C_5: \vartheta_i \in [0, 2\pi], \forall i \in \mathcal{N} = \{1, 2, \dots, N\}, \quad (15f)$$

$$C_6: \|\hat{\mathbf{t}}_l - \hat{\mathbf{t}}_j\|_2 \geq D, \forall l, j \in \mathcal{L}, \quad l \neq j, \quad (15g)$$

$$C_7: \hat{\mathbf{t}} \in \mathcal{C}_t, \quad (15h)$$

where P_t , R_{\min} , and D denote the available power budget, the minimum rate threshold desired for QoS assurance, and the minimum separation distance between MAs to avoid mutual coupling effects, respectively. Constraint C_1 is imposed to satisfy QoS requirements, whereas C_2 guarantees successful decoding of the common stream. Constraint C_4 enforces the unit-modulus condition on the reflecting elements of the RIS. Constraint C_6 ensures sufficient separation among MAs to prevent mutual coupling, while constraint C_7 restricts the MA positions to lie within the region \mathcal{C}_t .

III. PROPOSED SOLUTION FOR THE OPTIMIZATION PROBLEM

It is important to emphasize that the strong coupling among the optimization variables \hat{r}_m^c , \mathbf{p}_c , \mathbf{p}_m , Φ , and $\hat{\mathbf{t}}$ renders problem (P1) highly non-convex and intractable. To tackle this challenge, we develop an efficient iterative solution framework that successively updates the coupled resource-allocation variables through active beamforming design, RIS reflection optimization, and MAs position adaptation.

A. Updating Precoding Vectors \mathbf{p}_c and \mathbf{p}_m

Under fixed values of Φ and $\hat{\mathbf{t}}$, the optimization problem associated with the design of the transmit precoding vectors is formulated as follows:

$$\text{(P2)} \quad \max_{(\hat{r}_m^c, \mathbf{p}_c, \mathbf{p}_m)} \sum_{m=1}^M (\hat{r}_m^c + R_m^p), \quad (16a)$$

$$\text{s.t. } (15b) - (15d). \quad (16b)$$

It should be noted that problem (P2) is highly non-convex, owing to the non-convex nature of both its objective function and constraints.

Next, we define $\mathbf{P}_m = \mathbf{p}_m \mathbf{p}_m^H$ and $\mathbf{P}_c = \mathbf{p}_c \mathbf{p}_c^H$ as two positive semidefinite (PSD) matrices satisfying $\text{rank}(\mathbf{P}_m) = 1$ and $\text{rank}(\mathbf{P}_c) = 1$. To facilitate tractable optimization, a

vector of slack variables $\boldsymbol{\kappa}_m^p = [\kappa_1^p, \dots, \kappa_M^p]^T$ is introduced as follows.

$$\hat{r}_m^c + \kappa_m^p \geq R_{\min}, \forall m \in \mathcal{M}, \quad (17a)$$

$$\log_2 \left(1 + \frac{\hat{\mathbf{g}}_m^H \mathbf{P}_m \hat{\mathbf{g}}_m}{\sum_{\substack{i=1 \\ i \neq m}}^M \hat{\mathbf{g}}_m^H \mathbf{P}_i \hat{\mathbf{g}}_m + \hat{\sigma}_m^2} \right) \geq \kappa_m^p, \|\Delta \mathbf{g}_m\| \leq \hat{\varrho}_m, \quad (17b)$$

Further, to track the convexity of (17b), we define a vector of auxiliary variables $\boldsymbol{\zeta}_m^p = [\zeta_1^p, \dots, \zeta_M^p]^T$ as follows

$$\hat{\mathbf{g}}_m^H \mathbf{P}_m \hat{\mathbf{g}}_m \geq (2^{\kappa_m^p} - 1) \zeta_m^p, \forall \|\Delta \mathbf{g}_m\| \leq \hat{\varrho}_m, \quad (18a)$$

$$\sum_{\substack{i=1 \\ i \neq m}}^M \hat{\mathbf{g}}_m^H \mathbf{P}_i \hat{\mathbf{g}}_m + \hat{\sigma}_m^2 \leq \zeta_m^p, \forall \|\Delta \mathbf{g}_m\| \leq \hat{\varrho}_m, \quad (18b)$$

To address the CSI uncertainties in (18a) and (18b), we reformulate these constraints into equivalent linear matrix inequalities (LMIs) [35], yielding the following robust convex constraints:

$$\begin{bmatrix} \lambda_m^p \mathbf{I} + \mathbf{P}_m & \mathbf{P}_m \mathbf{g}_m \\ \mathbf{g}_m^H \mathbf{P}_m & \mathbf{g}_m^H \mathbf{P}_m \mathbf{g}_m - (2^{\kappa_m^p} - 1) \zeta_m^p - \lambda_m^p \hat{\varrho}_m^2 \end{bmatrix} \succeq \mathbf{0}, \quad (19)$$

and,

$$\begin{bmatrix} \mu_m^p \mathbf{I} - \left(\sum_{\substack{i=1 \\ i \neq m}}^M \mathbf{P}_i \right) & - \left(\sum_{\substack{i=1 \\ i \neq m}}^M \mathbf{P}_i \right) \mathbf{g}_m \\ - \mathbf{g}_m^H \left(\sum_{\substack{i=1 \\ i \neq m}}^M \mathbf{P}_i \right) & \zeta_m^p - \hat{\sigma}_m^2 - \mathbf{g}_m^H \left(\sum_{\substack{i=1 \\ i \neq m}}^M \mathbf{P}_i \right) \mathbf{g}_m - \mu_m^p \hat{\varrho}_m^2 \end{bmatrix} \succeq \mathbf{0}, \quad (20)$$

where $\boldsymbol{\lambda}_m^p = [\lambda_1^p, \dots, \lambda_M^p]^T \geq \mathbf{0}$ and $\boldsymbol{\mu}_m^p = [\mu_1^p, \dots, \mu_M^p]^T \geq \mathbf{0}$ are vectors of auxiliary variables.

Accordingly, to trace the convexity of (15c), we introduce a vector of slack variables $\boldsymbol{\beta}_m^c = [\beta_1^c, \dots, \beta_M^c]^T$ as follows

$$\hat{\mathbf{g}}_m^H \mathbf{P}_c \hat{\mathbf{g}}_m \geq (2^{(\sum_{m=1}^M \hat{r}_m^c)} - 1) \beta_m^c, \forall \|\Delta \mathbf{g}_m\| \leq \hat{\varrho}_m, \quad (21a)$$

$$\sum_{i=1}^M \hat{\mathbf{g}}_m^H \mathbf{P}_i \hat{\mathbf{g}}_m + \hat{\sigma}_m^2 \leq \beta_m^c, \forall \|\Delta \mathbf{g}_m\| \leq \hat{\varrho}_m, \quad (21b)$$

Next, we reformulate (21a) and (21b) into equivalent LMIs, resulting in the following convex constraints:

$$\begin{bmatrix} \lambda_m^c \mathbf{I} + \mathbf{P}_c & \mathbf{P}_c \mathbf{g}_m \\ \mathbf{g}_m^H \mathbf{P}_c & \mathbf{g}_m^H \mathbf{P}_c \mathbf{g}_m - \left(2 \left(\sum_{k=1}^M \hat{r}_k^c\right) - 1\right) \beta_m^c - \lambda_m^c \hat{\varrho}_m^2 \end{bmatrix} \succeq \mathbf{0},$$

(22)

$\forall m \in \mathcal{M}$,

$$\begin{bmatrix} \mu_m^c \mathbf{I} - \sum_{i=1}^M \mathbf{P}_i & - \left(\sum_{i=1}^M \mathbf{P}_i\right) \mathbf{g}_m \\ -\mathbf{g}_m^H \left(\sum_{i=1}^M \mathbf{P}_i\right) & \beta_m^c - \hat{\sigma}_m^2 - \mathbf{g}_m^H \left(\sum_{i=1}^M \mathbf{P}_i\right) \mathbf{g}_m - \mu_m^c \hat{\varrho}_m^2 \end{bmatrix} \succeq \mathbf{0},$$

(23)

where $\boldsymbol{\lambda}_m^c = [\lambda_1^c, \dots, \lambda_M^c]^T \succeq \mathbf{0}$ and $\boldsymbol{\mu}_m^c = [\mu_1^c, \dots, \mu_M^c]^T \succeq \mathbf{0}$ denote vectors of non-negative auxiliary variables.

Consequently, problem **(P2)** can be recast as follows

$$\text{(P3)} \quad \max_{\hat{\boldsymbol{\alpha}}} \sum_{m=1}^M \left(\hat{r}_m^c + \kappa_m^p \right), \quad (24a)$$

$$\text{s.t.} \quad \hat{r}_m^c + \kappa_m^p \geq R_{\min}, \quad \forall m \in \mathcal{M}, \quad (24b)$$

$$(19), (20), (22), (23), \quad (24c)$$

$$\text{tr}(\mathbf{P}_c) + \sum_{m=1}^M \text{tr}(\mathbf{P}_m) \leq P_t, \quad \forall m \in \mathcal{M}, \quad (24d)$$

$$\mathbf{P}_c \succeq \mathbf{0}, \mathbf{P}_m \succeq \mathbf{0}, \quad \forall m \in \mathcal{M}, \quad (24e)$$

$$\text{rank}(\mathbf{P}_c) = 1, \text{rank}(\mathbf{P}_m) = 1, \quad \forall m \in \mathcal{M}. \quad (24f)$$

where $\hat{\boldsymbol{\alpha}} = \{\hat{r}_m^c, \mathbf{P}_c, \mathbf{P}_m, \kappa_m^p, \zeta_m^p, \boldsymbol{\lambda}_m^c, \boldsymbol{\mu}_m^c, \beta_m^c, \boldsymbol{\lambda}_m^c, \boldsymbol{\mu}_m^c\}$.

It is important to emphasize that problem **(P3)** remains non-convex due to the rank-1 constraints in (24f). To handle this non-convexity, the rank-1 constraints are relaxed to transform **(P3)** into a convex formulation that can be solved efficiently. Moreover, if the resulting solutions \mathbf{P}_c and \mathbf{P}_m are of higher rank, feasible beamforming solutions are recovered through a rank-1 reconstruction procedure [36].

B. Updating RIS Reflection Matrix Φ

Under fixed values of precoding vectors \mathbf{p}_c , \mathbf{p}_m and MAs positions $\hat{\mathbf{t}}$, the optimization problem for computing Φ is formulated as follows

$$\text{(P4)} \quad \max_{(\hat{r}_m^c, \Phi)} \sum_{m=1}^M \left(\hat{r}_m^c + R_m^p \right), \quad (25a)$$

$$\text{s.t.} \quad (15b), (15c), (15e), (15f). \quad (25b)$$

We first reformulate problem **(P4)** into a tractable optimization form. Under the considered bounded CSI error model, where $\hat{\mathbf{g}}_m = \mathbf{g}_m + \Delta \mathbf{g}_m$ and $\|\Delta \mathbf{g}_m\| \leq \hat{\varrho}_m$, the second-order statistics of the channel can be expressed accordingly, and the covariance matrix of the effective channel is given by $\hat{\mathbf{G}}_m = \mathbf{G}_m + \Delta \mathbf{G}_m$ [34], where $\hat{\mathbf{G}}_m = \mathbb{E}\{\hat{\mathbf{g}}_m \hat{\mathbf{g}}_m^H\}$, $\mathbf{G}_m = \mathbb{E}\{\mathbf{g}_m \mathbf{g}_m^H\}$, and $\Delta \mathbf{G}_m = \mathbb{E}\{\Delta \mathbf{g}_m \Delta \mathbf{g}_m^H\}$ refer to the covariance matrices characterizing the effective channel, the estimated channel, and the estimation error, respectively.

Accordingly, Eqs. (10) and (12) can be updated as

$$\bar{R}_m^c = \log_2 \left(1 + \frac{\text{tr}(\mathbf{p}_c^H (\mathbf{G}_m + \Delta \mathbf{G}_m) \mathbf{p}_c)}{\sum_{i=1}^M \text{tr}(\mathbf{p}_i^H (\mathbf{G}_m + \Delta \mathbf{G}_m) \mathbf{p}_i) + \hat{\sigma}_m^2} \right),$$

$\forall m \in \mathcal{M}$, (26)

$$\bar{R}_m^p = \log_2 \left(1 + \frac{\text{tr}(\mathbf{p}_m^H (\mathbf{G}_m + \Delta \mathbf{G}_m) \mathbf{p}_m)}{\sum_{\substack{i=1 \\ i \neq m}}^M \text{tr}(\mathbf{p}_i^H (\mathbf{G}_m + \Delta \mathbf{G}_m) \mathbf{p}_i) + \hat{\sigma}_m^2} \right),$$

$\forall m \in \mathcal{M}$, (27)

Further, to tackle CSI uncertainties in Eqs. (26) and (27), We next present **Theorem 1** as follows:

Theorem 1: Let $\hat{\Psi}$ and $\hat{\Xi}$ denote Hermitian matrices, where $\hat{\Psi}$ is positive semidefinite with rank one. If $\hat{\Xi}$ satisfies the norm constraint $\|\hat{\Xi}\| \leq \hat{\varrho}^2$, then the following equality holds:

$$\max_{\|\hat{\Xi}\| \leq \hat{\varrho}^2} \text{tr}(\hat{\Psi} \hat{\Xi}) = \hat{\varrho}^2 \text{tr}(\hat{\Psi}). \quad (28)$$

Proof: The complete proof of **Theorem 1** can be found in Appendix A.

Next, we rewrite the quadratic terms as $\text{tr}(\mathbf{p}_m^H \Delta \mathbf{G}_m \mathbf{p}_m) = \text{tr}(\Delta \mathbf{G}_m \mathbf{P}_m)$ and $\text{tr}(\mathbf{p}_c^H \Delta \mathbf{G}_m \mathbf{p}_c) = \text{tr}(\Delta \mathbf{G}_m \mathbf{P}_c)$, where $\mathbf{P}_m = \mathbf{p}_m \mathbf{p}_m^H$ and $\mathbf{P}_c = \mathbf{p}_c \mathbf{p}_c^H$ are rank-one PSD matrices. By invoking **Theorem 1**, we can further obtain

$$\max_{\|\Delta \mathbf{G}_m\| \leq \hat{\varrho}^2} \text{tr}(\Delta \mathbf{G}_m \mathbf{P}_c) = \hat{\varrho}^2 \text{tr}(\mathbf{P}_c), \quad (29)$$

and,

$$\max_{\|\Delta \mathbf{G}_m\| \leq \hat{\varrho}^2} \text{tr}(\Delta \mathbf{G}_m \mathbf{P}_m) = \hat{\varrho}^2 \text{tr}(\mathbf{P}_m). \quad (30)$$

Further, we define a PSD matrix $\hat{\mathbf{V}} = \mathbf{v} \mathbf{v}^H$, satisfying $\hat{\mathbf{V}} \succeq \mathbf{0}$ and $\text{rank}(\hat{\mathbf{V}}) = 1$, where $\mathbf{v} = [e^{j\vartheta_1}, e^{j\vartheta_2}, \dots, e^{j\vartheta_N}]^T$. Thus, under the worst-case CSI assumption, and by exploiting (29) and (30), the expressions in (26) and (27) can be reformulated as

$$\hat{R}_m^c = \log_2 \left(1 + \frac{\text{tr}(\hat{\mathbf{V}} \hat{\mathbf{U}}_1) - \hat{\varrho}_m^2 \text{tr}(\mathbf{P}_c)}{\text{tr}(\hat{\mathbf{V}} \hat{\mathbf{U}}_2) + \hat{\varrho}_m^2 \text{tr}(\mathbf{S}_1) + \hat{\sigma}_m^2} \right), \quad (31)$$

and,

$$\hat{R}_m^p = \log_2 \left(1 + \frac{\text{tr}(\hat{\mathbf{V}} \hat{\mathbf{W}}_1) - \hat{\varrho}_m^2 \text{tr}(\mathbf{P}_m)}{\text{tr}(\hat{\mathbf{V}} \hat{\mathbf{W}}_2) + \hat{\varrho}_m^2 \text{tr}(\mathbf{S}_2) + \hat{\sigma}_m^2} \right), \quad (32)$$

where $\hat{\mathbf{U}}_1 = \mathbf{H}_{b,r} \mathbf{P}_c \mathbf{H}_{b,r}^H \mathbf{h}_{r,m} \mathbf{h}_{r,m}^H$, $\mathbf{S}_1 = \sum_{i=1}^M \mathbf{P}_i$, $\hat{\mathbf{U}}_2 = \mathbf{H}_{b,r} \mathbf{S}_1 \mathbf{H}_{b,r}^H \mathbf{h}_{r,m} \mathbf{h}_{r,m}^H$, $\hat{\mathbf{W}}_1 = \mathbf{H}_{b,r} \mathbf{P}_m \mathbf{H}_{b,r}^H \mathbf{h}_{r,m} \mathbf{h}_{r,m}^H$, $\mathbf{S}_2 = \sum_{\substack{i=1 \\ i \neq m}}^M \mathbf{P}_i$, $\hat{\mathbf{W}}_2 = \mathbf{H}_{b,r} \mathbf{S}_2 \mathbf{H}_{b,r}^H \mathbf{h}_{r,m} \mathbf{h}_{r,m}^H$.

Accordingly, the optimization problem **(P4)** can be equiva-

lently expressed as follows

$$\text{(P5)} \quad \max_{(\hat{r}_m^c, \hat{\mathbf{V}})} \sum_{m=1}^M \left(\hat{r}_m^c + \hat{R}_m^p \right), \quad (33a)$$

$$\text{s.t.} \quad \hat{r}_m^c + \hat{R}_m^p \geq R_{min}, \forall m \in \mathcal{M}, \quad (33b)$$

$$\sum_{m=1}^M \hat{r}_m^c \leq \hat{R}_m^c, \forall m \in \mathcal{M}, \quad (33c)$$

$$\hat{\mathbf{V}} \succeq \mathbf{0}, \quad (33d)$$

$$\text{rank}(\hat{\mathbf{V}}) = 1. \quad (33e)$$

Next, to trace the convexity of **(P5)**, we introduce a vector of slack variables $\varpi_m^p = [\varpi_1^p, \dots, \varpi_M^p]^T$, defined as follows

$$\hat{r}_m^c + \hat{R}_m^p \geq \varpi_m^p, \forall m \in \mathcal{M}. \quad (34)$$

Further, Eq. (34) can be expressed as follows

$$\begin{aligned} & \hat{r}_m^c + \log_2 \left(\text{tr} \left(\hat{\mathbf{V}} \hat{\mathbf{W}}_1 \right) - \hat{\varrho}_m^2 \text{tr} \left(\mathbf{P}_m \right) + \text{tr} \left(\hat{\mathbf{V}} \hat{\mathbf{W}}_2 \right) \right. \\ & \left. + \hat{\varrho}_m^2 \text{tr} \left(\mathbf{S}_2 \right) + \hat{\sigma}_m^2 \right) - \log_2 \left(\text{tr} \left(\hat{\mathbf{V}} \hat{\mathbf{W}}_2 \right) + \hat{\varrho}_m^2 \text{tr} \left(\mathbf{S}_2 \right) \right. \\ & \left. + \hat{\sigma}_m^2 \right) \geq \varpi_m^p, \forall m \in \mathcal{M}. \end{aligned} \quad (35)$$

Since (35) remains non-convex, as it involves the difference of two concave functions. Thus, we replace the non-convex term with its first-order lower-bound constructed around a given point $\hat{\mathbf{V}}^{(r)}$, as follows.

$$\begin{aligned} & \hat{r}_m^c + \log_2 \left(\text{tr} \left(\hat{\mathbf{V}} \hat{\mathbf{W}}_1 \right) - \hat{\varrho}_m^2 \text{tr} \left(\mathbf{P}_m \right) + \text{tr} \left(\hat{\mathbf{V}} \hat{\mathbf{W}}_2 \right) \right. \\ & \left. + \hat{\varrho}_m^2 \text{tr} \left(\mathbf{S}_2 \right) + \hat{\sigma}_m^2 \right) - \Pi_m(\hat{\mathbf{V}}) \geq \varpi_m^p, \forall m \in \mathcal{M}, \end{aligned} \quad (36)$$

where $\Pi_m(\hat{\mathbf{V}})$ denotes the first-order lower-bound, which is given in (37) at the top of the next page.

Further, to facilitate the convexification of constraint (33c), it can be rewritten as follows:

$$\begin{aligned} & \log_2 \left(\text{tr} \left(\hat{\mathbf{V}} \hat{\mathbf{U}}_1 \right) - \hat{\varrho}_m^2 \text{tr} \left(\mathbf{P}_c \right) + \text{tr} \left(\hat{\mathbf{V}} \hat{\mathbf{U}}_2 \right) + \hat{\varrho}_m^2 \text{tr} \left(\mathbf{S}_1 \right) \right. \\ & \left. + \hat{\sigma}_m^2 \right) - \log_2 \left(\text{tr} \left(\hat{\mathbf{V}} \hat{\mathbf{U}}_2 \right) + \hat{\varrho}_m^2 \text{tr} \left(\mathbf{S}_1 \right) + \hat{\sigma}_m^2 \right) \\ & \geq \sum_{m \in \mathcal{M}} \hat{r}_m^c, \quad \forall m \in \mathcal{M}. \end{aligned} \quad (38)$$

It is important to note that the non-convexity of (38) arises from the second logarithmic term. Thus, we employ first-order lower-bound around a given point $\hat{\mathbf{V}}^{(r)}$, as follows

$$\begin{aligned} & \log_2 \left(\text{tr} \left(\hat{\mathbf{V}} \hat{\mathbf{U}}_1 \right) - \hat{\varrho}_m^2 \text{tr} \left(\mathbf{P}_c \right) + \text{tr} \left(\hat{\mathbf{V}} \hat{\mathbf{U}}_2 \right) + \hat{\varrho}_m^2 \text{tr} \left(\mathbf{S}_1 \right) \right. \\ & \left. + \hat{\sigma}_m^2 \right) - \Pi_c(\hat{\mathbf{V}}) \geq \sum_{m \in \mathcal{M}} \hat{r}_m^c, \quad \forall m \in \mathcal{M}. \end{aligned} \quad (39)$$

where $\Pi_c(\hat{\mathbf{V}})$ denotes the first-order lower bound given in (40) at the top of the next page.

Finally, problem **(P5)** is equivalently reformulated as follows.

$$\text{(P6)} \quad \max_{(\hat{r}_m^c, \varpi_m^p, \hat{\mathbf{V}})} \sum_{m=1}^M \varpi_m^p, \quad (41a)$$

$$\text{s.t.} \quad \varpi_m^p \geq R_{min}, \forall m \in \mathcal{M}, \quad (41b)$$

$$\hat{\mathbf{V}} \succeq \mathbf{0}, \quad (41c)$$

$$\text{rank}(\hat{\mathbf{V}}) = 1. \quad (41d)$$

$$(36), (39). \quad (41e)$$

It is worth noting that the presence of rank-one constraint in (41d) renders problem **(P6)** non-convex. To address this issue, the rank-1 constraints are relaxed by reformulating problem **(P6)** into a tractable convex formulation. Moreover, if the resulting solution is not rank one, a rank-one recovery procedure is applied to obtain a feasible passive beamforming configuration [36].

C. Updating MAs Positions $\hat{\mathbf{t}}$

For given \mathbf{p}_c , \mathbf{p}_m , and Φ , and by leveraging (31) and (32), the optimization problem for determining the MAs positions $\hat{\mathbf{t}}$ can be formulated as follows

$$\text{(P7)} \quad \max_{(\hat{r}_m^c, \hat{\mathbf{t}})} \sum_{m=1}^M \left(\hat{r}_m^c + \hat{R}_m^p \right), \quad (42a)$$

$$\text{s.t.} \quad \hat{r}_m^c + \hat{R}_m^p \geq R_{min}, \forall m \in \mathcal{M}, \quad (42b)$$

$$\sum_{m=1}^M \hat{r}_m^c \leq \hat{R}_m^c, \forall m \in \mathcal{M}, \quad (42c)$$

$$\left\| \hat{\mathbf{t}}_l - \hat{\mathbf{t}}_j \right\|_2 \geq D, \forall l, j \in \mathcal{L}, \quad l \neq j, \quad (42d)$$

$$\hat{\mathbf{t}} \in \mathcal{C}_t. \quad (42e)$$

It is worth emphasizing that **(P7)** is computationally challenging since $\mathbf{H}_{b,r}(\hat{\mathbf{t}})$ is a nonlinear function of $\hat{\mathbf{t}}$ involving complex exponential functions, and the MAs position variables $\{\hat{\mathbf{t}}_l\}_{l=1}^L$ are jointly coupled. To this end, we solve **(P7)** in an alternating manner. Specifically, in each iteration, we optimize the position of one antenna while keeping the positions of the other antennas fixed. This procedure is repeated until a convergence criterion is satisfied.

Next, we focus on optimizing the position of the l -th MA, $\hat{\mathbf{t}}_l$, while keeping the positions of other MAs $\{\hat{\mathbf{t}}_j\}_{j=1, j \neq l}^L$ fixed. Accordingly, to optimize $\hat{\mathbf{t}}_l$, we introduce a slack-variable vector $\Upsilon_m^p = [\Upsilon_1^p, \dots, \Upsilon_M^p]^T$ as follows

$$\hat{R}_m^p \geq \Upsilon_m^p, \forall m \in \mathcal{M}. \quad (43)$$

To track the convexification of (43), its convex surrogate can be computed as

$$\hat{R}_m^{p(r)} + \left(\nabla_{\hat{\mathbf{t}}_l} \hat{R}_m^{p(r)} \right)^T \left(\hat{\mathbf{t}}_l - \hat{\mathbf{t}}_l^{(r)} \right) \geq \Upsilon_m^p, \forall m \in \mathcal{M}. \quad (44)$$

where $\nabla_{\hat{\mathbf{t}}_l} \hat{R}_m^{p(r)}$ denotes the gradient of $\hat{R}_m^{p(r)}$ with respect to $\hat{\mathbf{t}}_l$ at the r -th iteration, which can be computed using the chain

$$\Pi_m(\widehat{\mathbf{V}}) = \log_2 \left(\text{tr} \left(\widehat{\mathbf{V}}^{(r)} \widehat{\mathbf{W}}_2 \right) + \widehat{\varrho}_m^2 \text{tr}(\mathbf{S}_2) + \widehat{\sigma}_m^2 \right) + \text{tr} \left(\frac{\widehat{\mathbf{W}}_2 (\widehat{\mathbf{V}} - \widehat{\mathbf{V}}^{(r)})}{\left(\text{tr} \left(\widehat{\mathbf{V}}^{(r)} \widehat{\mathbf{W}}_2 \right) + \widehat{\varrho}_m^2 \text{tr}(\mathbf{S}_2) + \widehat{\sigma}_m^2 \right) \ln 2} \right), \quad (37)$$

$$\Pi_c(\widehat{\mathbf{V}}) = \log_2 \left(\text{tr} \left(\widehat{\mathbf{V}}^{(r)} \widehat{\mathbf{U}}_2 \right) + \widehat{\varrho}_m^2 \text{tr}(\mathbf{S}_1) + \widehat{\sigma}_m^2 \right) + \text{tr} \left(\frac{\widehat{\mathbf{U}}_2 (\widehat{\mathbf{V}} - \widehat{\mathbf{V}}^{(r)})}{\left(\text{tr} \left(\widehat{\mathbf{V}}^{(r)} \widehat{\mathbf{U}}_2 \right) + \widehat{\varrho}_m^2 \text{tr}(\mathbf{S}_1) + \widehat{\sigma}_m^2 \right) \ln 2} \right). \quad (40)$$

rule. Accordingly, to trace the convexity of (42c), we can write as

$$\widehat{R}_m^{c(r)} + \left(\nabla_{\widehat{\mathbf{t}}_l} \widehat{R}_m^{c(r)} \right)^T \left(\widehat{\mathbf{t}}_l - \widehat{\mathbf{t}}_l^{(r)} \right) \geq \sum_{m \in \mathcal{M}} \widehat{r}_m^c, \quad \forall m \in \mathcal{M}. \quad (45)$$

where $\nabla_{\widehat{\mathbf{t}}_l} \widehat{R}_m^{c(r)}$ denotes the gradient of $\widehat{R}_m^{c(r)}$ at the r -th iteration. Subsequently, it is important to note that constraint (42d) is non-convex, as it imposes a lower bound on a convex function. To address this issue, we compute its first-order lower bound given as follows

$$\frac{1}{\left\| \widehat{\mathbf{t}}_l^{(r)} - \widehat{\mathbf{t}}_j \right\|_2} \left(\widehat{\mathbf{t}}_l^{(r)} - \widehat{\mathbf{t}}_j \right)^T \left(\widehat{\mathbf{t}}_l - \widehat{\mathbf{t}}_j \right) \geq D, \forall l \neq j, \quad (46)$$

where $\widehat{\mathbf{t}}_l^{(r)}$ denotes the value of $\widehat{\mathbf{t}}_l$ at the r -th iteration. The detailed derivation of (46) is provided in Appendix B.

Finally, the optimization problem for updating the MAs positions can be reformulated as follows

$$\text{(P8)} \quad \max_{(\widehat{r}_m^c, \widehat{\mathbf{t}}_l, \Upsilon_m^p)} \sum_{m=1}^M \left(\widehat{r}_m^c + \Upsilon_m^p \right), \quad (47a)$$

$$\text{s.t.} \quad \widehat{r}_m^c + \Upsilon_m^p \geq R_{\min}, \forall m \in \mathcal{M}, \quad (47b)$$

$$\frac{\left(\widehat{\mathbf{t}}_l^{(r)} - \widehat{\mathbf{t}}_j \right)^T}{\left\| \widehat{\mathbf{t}}_l^{(r)} - \widehat{\mathbf{t}}_j \right\|_2} \left(\widehat{\mathbf{t}}_l - \widehat{\mathbf{t}}_j \right) \geq D, \forall l \neq j, \quad (47c)$$

$$\widehat{\mathbf{t}} \in \mathcal{C}_t, \quad (47d)$$

$$(44), (45), \quad (47e)$$

which results in a convex optimization problem that is efficiently solvable using CVX with the MOSEK solver.

D. Complexity and Convergence Analysis of the Proposed Robust Algorithm

1) *Computational Complexity*: For the system under consideration, an iterative robust optimization framework is proposed in **Algorithm 1**. The main computational complexity of **Algorithm 1** results from the iterative solutions of **(P3)**, **(P6)**, and **(P8)**. Specifically, subproblems **(P3)** and **(P6)** are solved using the CVX framework based on interior-point techniques. This leads to computational complexity on the order of $\mathcal{O}(\varepsilon_1 L^{3.5})$ and $\mathcal{O}(\varepsilon_2 N^{3.5})$, respectively [23], [37], where ε_1 and ε_2 represent the number of iterations needed for **Stage 1** and **Stage 2** convergence, respectively. Further, the MAs positions are computed by solving subproblem **(P8)** in an alternating manner,

Algorithm 1 Proposed Robust Optimization Algorithm

- 1: **Initialization**: Initialize $\widehat{\mathbf{P}}_c, \widehat{\mathbf{P}}_m, \widehat{\Phi}, \widehat{\mathbf{V}}, \widehat{\mathbf{t}}, \widehat{\Psi}_{q,x}^p, \kappa_m^p, \zeta_m^p, \lambda_m^p, \mu_m^p, \beta_m^c, \lambda_m^c, \mu_m^c, \varpi_m^p$, and Υ_m^p .
 - 2: **Stage 1**: Optimization of $\mathbf{P}_c, \mathbf{P}_m$
 - 3: **while** the algorithm has not converged and the iteration index $\leq \widehat{\chi}_{\max}$ **do**
 - 4: **while** convergence is not achieved and iteration index $\leq \varepsilon_1$ **do**
 - 5: Compute $\mathbf{P}_c, \mathbf{P}_m$, and by solving **(P3)**
 - 6: **if** $\text{rank}(\mathbf{P}_c)=1$ and $\text{rank}(\mathbf{P}_m)=1$ **then**
 - 7: Obtain \mathbf{p}_c and \mathbf{p}_q using SVD of \mathbf{P}_c and \mathbf{P}_q
 - 8: **else**
 - 9: Apply Gaussian randomization
 - 10: **end if**
 - 11: Update $\widehat{\mathbf{P}}_c \leftarrow \mathbf{P}_c$ and $\widehat{\mathbf{P}}_m \leftarrow \mathbf{P}_m$
 - 12: **end while**
 - 13: **Stage 2**: Optimization of Φ
 - 14: **while** convergence is not achieved and iteration index $\leq \varepsilon_2$ **do**
 - 15: Compute $\widehat{\mathbf{V}}$ by solving the problem **(P6)**
 - 16: **if** $\text{rank}(\widehat{\mathbf{V}})=1$ **then**
 - 17: Obtain \mathbf{v} using SVD of $\widehat{\mathbf{V}}$
 - 18: **else**
 - 19: Apply Gaussian randomization
 - 20: **end if**
 - 21: Update $\widehat{\mathbf{V}} \leftarrow \widehat{\mathbf{V}}$
 - 22: **end while**
 - 23: **Stage 3**: Optimization of $\widehat{\mathbf{t}}$
 - 24: **while** convergence is not achieved and iteration index $\leq \varepsilon_3$ **do**
 - 25: Update MAs positions $\widehat{\mathbf{t}}$ by solving the problem **(P8)**
 - 26: Update $\widehat{\mathbf{t}} \leftarrow \widehat{\mathbf{t}}$
 - 27: **end while**
 - 28: **end while**
 - 29: **return** $\mathbf{p}_c^*, \mathbf{p}_m^*, \Phi^*, \widehat{\mathbf{t}}^*$
 - 30: **return** $\mathbf{p}_c^*, \mathbf{p}_m^*, \Phi^*, \widehat{\mathbf{t}}^*$
-

with computational complexity $\mathcal{O}(\varepsilon_3 L)$, where ε_3 represents the number of iterations needed for **Stage 3** to converge. As a result, the total computational complexity of **Algorithm 1** can be written as $\mathcal{O}(\widehat{\chi}_{\max} (\varepsilon_1 L^{3.5} + \varepsilon_2 N^{3.5} + \varepsilon_3 L))$, where $\widehat{\chi}_{\max}$ is the total number of outer iterations needed for

Algorithm 1 to converge.

2) *Convergence Analysis*: Let $\mathbf{p}_c^{(r)}$, $\mathbf{p}_m^{(r)}$, $\Phi^{(r)}$, and $\hat{\mathbf{t}}^{(r)}$ denote the optimized variables obtained at the r -th iteration. Then, $\Xi(\mathbf{p}_c^{(r)}, \mathbf{p}_m^{(r)}, \Phi^{(r)}, \hat{\mathbf{t}}^{(r)})$ denotes the associated objective function.

At iteration r in **Stage 1**, for given $\Phi^{(r)}$ and $\hat{\mathbf{t}}^{(r)}$, the precoding vectors are updated using convex surrogates that are tight around the current point and preserve first-order optimality. Thus, we obtain

$$\begin{aligned} \Xi(\mathbf{p}_c^{(r+1)}, \mathbf{p}_m^{(r+1)}, \Phi^{(r)}, \hat{\mathbf{t}}^{(r)}) &\geq \\ \Xi(\mathbf{p}_c^{(r)}, \mathbf{p}_m^{(r)}, \Phi^{(r)}, \hat{\mathbf{t}}^{(r)}) &. \end{aligned} \quad (48)$$

Next, in **Stage 2**, for fixed precoding vectors $\mathbf{p}_c^{(r+1)}$, $\mathbf{p}_m^{(r+1)}$ and MAs positions $\hat{\mathbf{t}}^{(r)}$, the passive beamforming scattering matrix is updated by solving the corresponding convexified subproblem. Therefore, the following inequality holds

$$\begin{aligned} \Xi(\mathbf{p}_c^{(r+1)}, \mathbf{p}_m^{(r+1)}, \Phi^{(r+1)}, \hat{\mathbf{t}}^{(r)}) &\geq \\ \Xi(\mathbf{p}_c^{(r+1)}, \mathbf{p}_m^{(r+1)}, \Phi^{(r)}, \hat{\mathbf{t}}^{(r)}) &. \end{aligned} \quad (49)$$

Subsequently, in **Stage 3**, the MAs positions are updated for fixed precoding vectors $\mathbf{p}_c^{(r+1)}$, $\mathbf{p}_m^{(r+1)}$ and passive beamforming matrix $\Phi^{(r+1)}$. Thus, we obtain

$$\begin{aligned} \Xi(\mathbf{p}_c^{(r+1)}, \mathbf{p}_m^{(r+1)}, \Phi^{(r+1)}, \hat{\mathbf{t}}^{(r+1)}) &\geq \\ \Xi(\mathbf{p}_c^{(r+1)}, \mathbf{p}_m^{(r+1)}, \Phi^{(r+1)}, \hat{\mathbf{t}}^{(r)}) &. \end{aligned} \quad (50)$$

Thus, by combining Eqs. (48), (49), and (50), we obtain

$$\begin{aligned} \Xi(\mathbf{p}_c^{(r+1)}, \mathbf{p}_m^{(r+1)}, \Phi^{(r+1)}, \hat{\mathbf{t}}^{(r+1)}) &\geq \\ \Xi(\mathbf{p}_c^{(r)}, \mathbf{p}_m^{(r)}, \Phi^{(r)}, \hat{\mathbf{t}}^{(r)}) &. \end{aligned} \quad (51)$$

Consequently, the derived sequence of inequalities establishes that the objective function is monotonically non-decreasing over the iterations of **Algorithm 1**, thereby guaranteeing its convergence.

IV. SIMULATION RESULTS AND PERFORMANCE ANALYSIS

In this work, the performance of the considered system is evaluated through numerical simulations. As illustrated in Fig. 2, the BS and RIS are located at coordinates (0 m, 0 m) and (30 m, 10 m), respectively. Moreover, the users are randomly distributed within a circular region of radius 10 m, centered at (30 m, 0 m). Further, the planar far-field geometric channel model is adopted with $L_t = L_r$, where the elevation and azimuth angles of all propagation paths, ϕ_i^e , φ_j^e , ϕ_i^a , and φ_j^a , are uniformly distributed over $[0, \pi]$. Unless otherwise specified, all simulation results are averaged over 10^4 independent channel realizations. It is assumed that line-of-sight (LoS) links exist for both the BS–RIS and RIS–user channels. Accordingly, the diagonal elements of the BS–RIS path response matrix $\mathbf{\Lambda}$ are modeled as $\Lambda[1, 1] \sim \mathcal{CN}\left(0, \frac{\hat{\varsigma}}{\hat{\varsigma}+1} \mathcal{P}_0 \left(\frac{d}{d_0}\right)^{-\hat{\nu}_1}\right)$ and $\Lambda[i, i] \sim \mathcal{CN}\left(0, \frac{1}{\hat{\varsigma}+1} \mathcal{P}_0 \left(\frac{d}{d_0}\right)^{-\hat{\nu}_1} / (L-1)\right)$ for $i =$

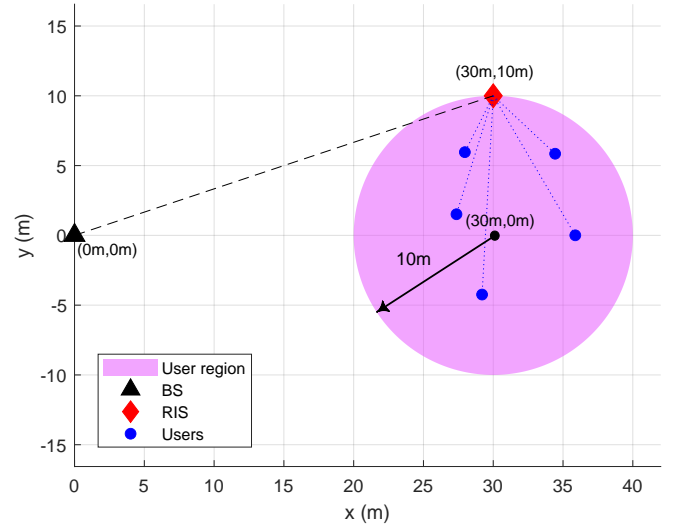


Fig. 2: Simulation environment.

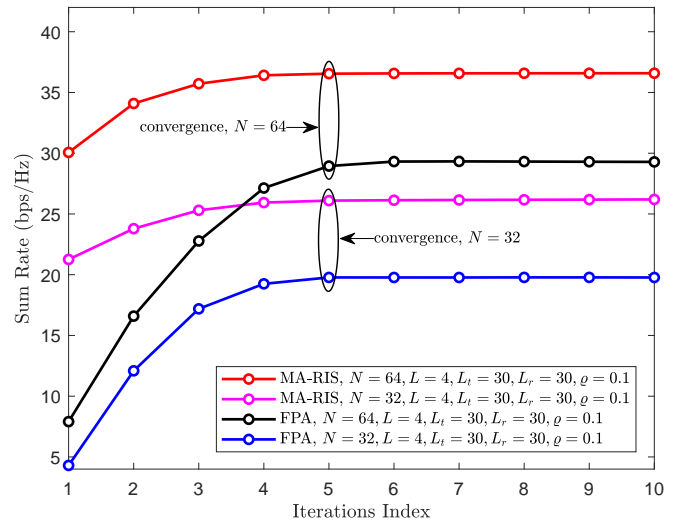


Fig. 3: System convergence for different number of RIS elements.

2, 3, ..., L, where $\hat{\varsigma}$ and $\hat{\nu}_1$ denote the Rician factor and path-loss exponent, respectively, and \mathcal{P}_0 represents the average channel power gain at a reference distance $d_0 = 1$ m. Moreover, the RIS–user channels $\mathbf{h}_{r,m} \in \mathbb{C}^{N \times 1}$ are independent of the MA positions and are modeled using Rician fading to account for both LoS and non-line-of-sight (NLoS) components, where path-loss exponent for RIS–user link is denoted as $\hat{\nu}_2$. Unless otherwise specified, the main simulation parameters are configured as follows: $\hat{\nu}_1 = 2$, $\hat{\nu}_2 = 2.5$, $\mathcal{P}_0 = -30$ dB, $\mathbf{C}_t = \left[-\frac{A}{2}, \frac{A}{2}\right] \times \left[-\frac{A}{2}, \frac{A}{2}\right]$, $A = 3\lambda$ with $\lambda = 0.1$ m [13], $\hat{\sigma}_m^2 = -80$ dBm, $R_{\min} = 1$ bps/Hz, $D = \lambda/2$, $P_t = 15$ Watts, $\varsigma = 3$, $M = 3$, and $\hat{\varrho}_m^2 = \varrho \|\mathbf{G}_m\|$, where $\varrho \in [0, 1]$ [38].

The convergence performance of the proposed optimization framework is shown in Figs. 3–5 with different system parameters. Specifically, Fig. 3 shows the convergence performance of the proposed scheme, denoted as MA-RIS, and the fixed-position antenna (FPA) benchmark for different values of the number of RIS elements N . Also, Fig. 4 shows the

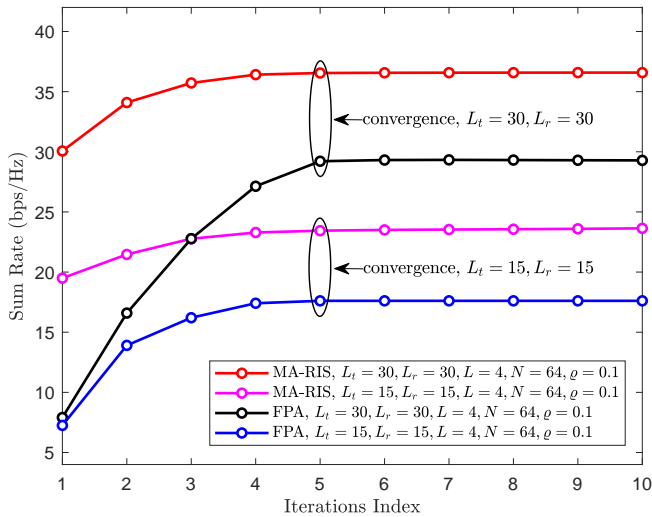


Fig. 4: System convergence for different number transmit and receive paths.

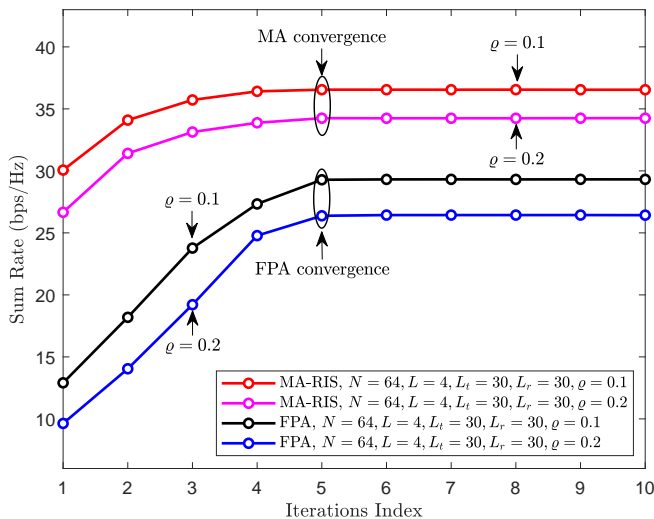


Fig. 5: System convergence for different levels of channel uncertainty.

convergence comparison of the proposed scheme and the FPA benchmark for different values of L_t and L_r . Moreover, Fig. 5 illustrates the convergence performance of the proposed scheme and its FPA counterpart for different values of the channel uncertainty parameter ϱ . From the simulation results in Figs. 3–5, it is observed that the proposed scheme always outperforms the FPA benchmark for all values of N , L_t , L_r , and ϱ , while achieving stable convergence within a practical number of iterations.

Fig. 6 exhibits the impact of the increasing number of RIS elements N on the system sum-rate under different values of ϱ . It can be seen that the sum-rate performance improves with an increase in N . This is due to the increased effective channel gain and the additional spatial degrees of freedom provided by the RIS, which improve the effectiveness of passive beamforming. Also, it is clear that the proposed scheme always outperforms the FPA benchmark in terms of sum-rate performance for all values of N and ϱ . On the other

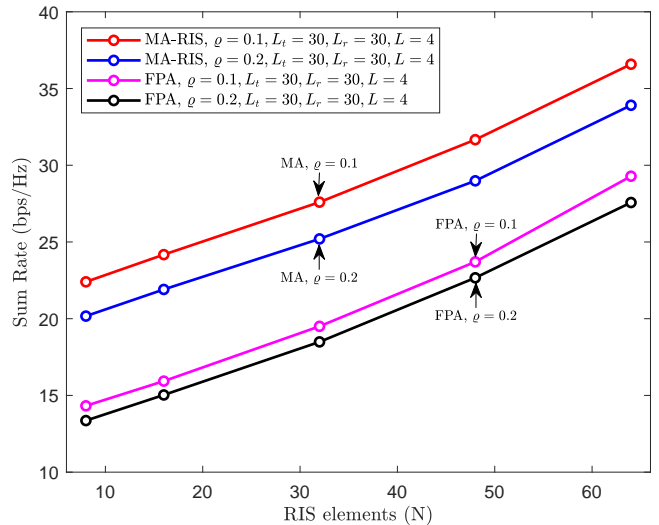


Fig. 6: Sum-rate performance across increasing values of N .

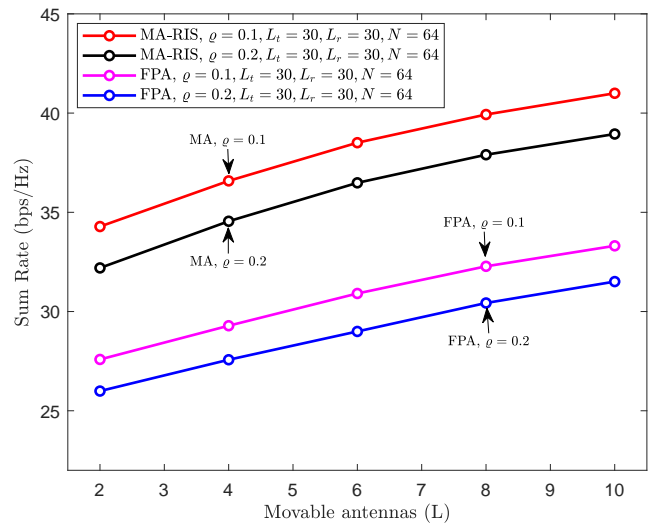


Fig. 7: Sum-rate performance for different number of MAs L .

hand, the sum-rate performance decreases with an increase in ϱ . This can be attributed to the negative effect of high channel uncertainty on channel estimation accuracy.

Fig. 7 shows the effect of the number of movable antennas L on the sum-rate performance of the system for different values of the channel uncertainty parameter ϱ . It is observed that the increase in L results in a guaranteed improvement in the sum-rate performance. This is because the movable antennas introduce an extra degree of spatial freedom that helps in more optimal positioning of the antennas and, hence, a better beamforming gain at the BS. This results in a better focusing of the signal power towards the desired receivers. However, the sum-rate performance deteriorates with an increase in ϱ due to the negative effect of the increased channel uncertainty on the SINR values.

Fig. 8 depicts the variation of the achievable system sum-rate with respect to the transmit power budget P_t under different levels of channel uncertainty ϱ . As P_t increases, a steady improvement in sum-rate performance is observed, which can

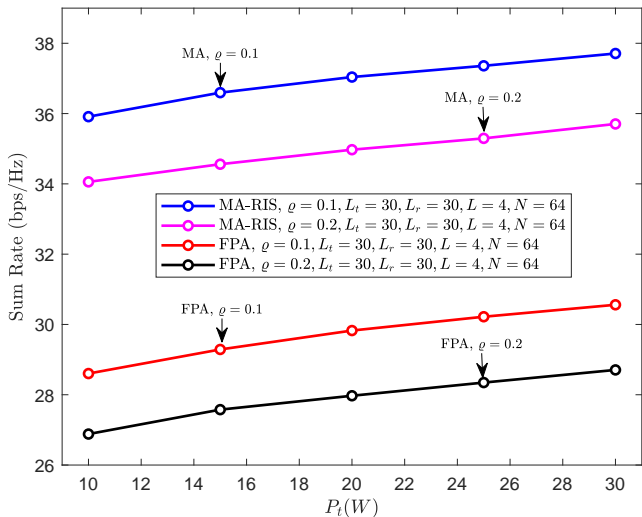


Fig. 8: Performance analysis for increasing power-budget P_t .

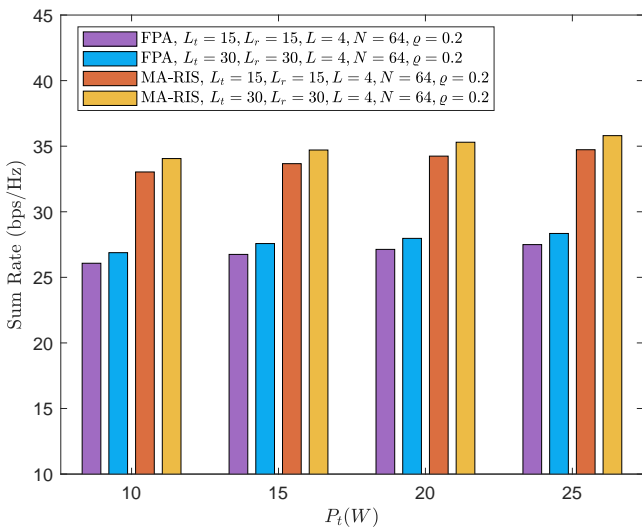


Fig. 9: System performance for different values of L_t and L_r .

be attributed to the enhanced received signal strength and the resulting increase in the SINR at the users. Moreover, the proposed scheme consistently achieves higher sum-rate performance than the FPA benchmark for all considered values of P_t and ρ , demonstrating its superior robustness and power utilization efficiency under imperfect CSI conditions. Likewise, Fig. 9 also shows the sum-rate performance of the considered system as a function of the transmit power budget P_t for various values of the number of transmit and receive paths, L_t and L_r , using the planar far-field response channel model. It is clear that increasing the values of L_t and L_r results in a significant improvement in the achievable sum-rate performance. This is because the stronger small-scale fading associated with the increased number of propagation paths, results in increased spatial channel variations, which can be leveraged using movable antennas to improve the sum-rate performance. Moreover, Fig. 10 presents a comparative evaluation of the proposed scheme and its SDMA-based

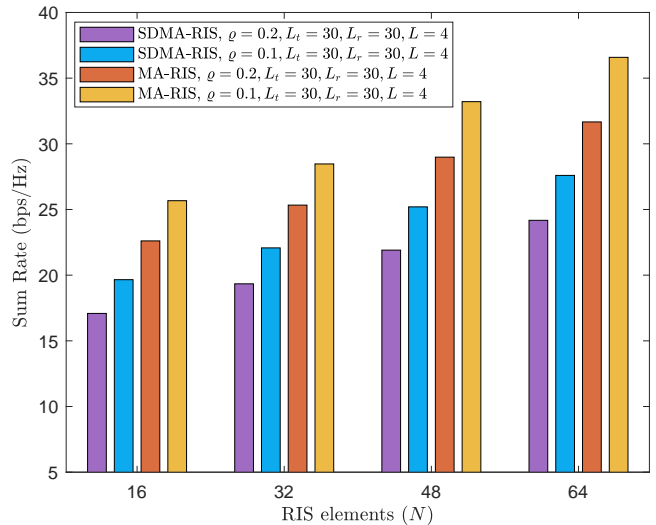


Fig. 10: Performance comparison of proposed scheme and its SDMA benchmark.

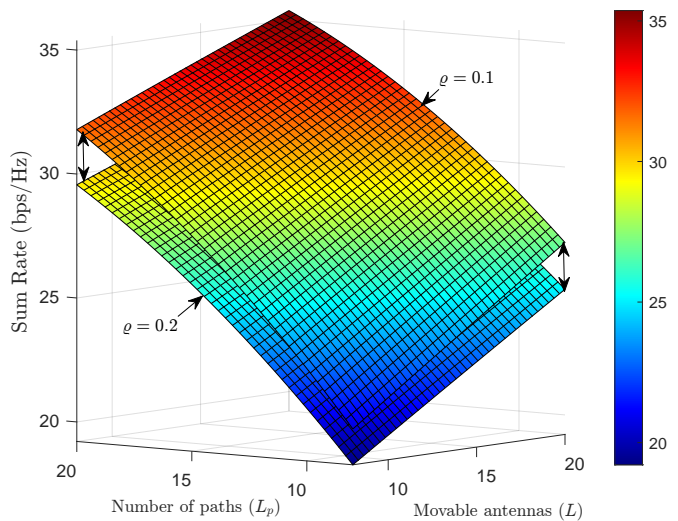


Fig. 11: Joint effect of L_p and L on system sum-rate performance.

benchmark, referred to as SDMA-RIS, under varying numbers of RIS elements N and different channel uncertainty levels ρ . The results clearly indicate that the proposed approach consistently achieves higher sum-rate performance across all considered values of N and ρ .

Finally, Fig. 11 shows the joint impact of the number of movable antennas L and the number of transmit and receive paths ($L_t = L_r = L_p$) on the achievable system sum-rate under different levels of channel uncertainty ρ . The numerical results indicate that the number of propagation paths L_p has a more significant effect on the sum-rate than the number of movable antennas L . This is because increasing L_p directly introduces additional propagation components into the channel, thereby altering the channel composition by adding more path terms with independent gains and phases and providing more diverse phase contributions that can be constructively combined to enhance the system sum-rate. In contrast, increasing the number of movable antennas does not create new

propagation components; instead, it only enables the system to exploit the existing paths at different spatial locations. Consequently, the achievable sum-rate is more sensitive to L_p than to the number of movable antennas.

V. CONCLUSION

This paper proposed a robust joint resource allocation framework for an RIS-empowered MAs-enabled multi-user RSMA downlink system under channel estimation errors. By jointly exploiting the spatial adaptability of MAs, the propagation reconfigurability of RIS, and the interference management capability of RSMA, the proposed framework enhances the system sum-rate while satisfying QoS requirements in the absence of direct communication links. In particular, the spatial adaptability of MAs introduces a coupled robust optimization structure in which CSI uncertainty jointly affects beamforming design and antenna position adaptation. To address this challenge, an efficient iterative optimization framework was developed to jointly optimize active beamforming, RIS reflection control, common-rate allocation, and MAs positions under bounded CSI uncertainty conditions, thereby enabling robust and reliable communication performance in practical wireless environments. Finally, numerical results demonstrated that the proposed framework achieves significant sum-rate gains and enhanced robustness compared with benchmark schemes, while also exhibiting fast and stable convergence behavior. The proposed framework provides useful insights into the design of robust and spatially adaptive wireless systems, and may serve as a promising foundation for future intelligent 6G communication networks operating under dynamic and imperfect CSI conditions.

APPENDIX A

Consider two complex matrices $\hat{\mathbf{\Lambda}}$ and $\hat{\mathbf{\Omega}}$ satisfying the norm constraint $\|\hat{\mathbf{\Lambda}}\| \leq 1$. Under this condition, the inner product $\langle \hat{\mathbf{\Lambda}}, \hat{\mathbf{\Omega}} \rangle$ achieves its maximum value at the dual norm of $\hat{\mathbf{\Omega}}$, which can be expressed as

$$\max_{\|\hat{\mathbf{\Lambda}}\| \leq 1} \langle \hat{\mathbf{\Lambda}}, \hat{\mathbf{\Omega}} \rangle = \|\hat{\mathbf{\Omega}}\|_{\text{dual}}. \quad (52)$$

Based on (52), the following inequality immediately follows:

$$\text{tr}(\hat{\mathbf{\Omega}}^H \hat{\mathbf{\Lambda}}) \leq \|\hat{\mathbf{\Lambda}}\| \|\hat{\mathbf{\Omega}}\|_{\text{dual}}, \quad (53)$$

where $\|\cdot\|_{\text{dual}}$ denotes the dual norm corresponding to the adopted matrix norm.

Now, consider two Hermitian matrices $\hat{\mathbf{\Psi}}$ and $\hat{\mathbf{\Xi}}$ satisfying the bounded constraint $\|\hat{\mathbf{\Xi}}\| \leq \hat{\varrho}^2$. Using (53), we obtain

$$\text{tr}(\hat{\mathbf{\Psi}} \hat{\mathbf{\Xi}}) \leq \|\hat{\mathbf{\Xi}}\| \|\hat{\mathbf{\Psi}}\|_{\text{dual}} \leq \hat{\varrho}^2 \|\hat{\mathbf{\Psi}}\|_{\text{dual}}, \quad (54)$$

As a result, we can write as

$$\max_{\|\hat{\mathbf{\Xi}}\| \leq \hat{\varrho}^2} \text{tr}(\hat{\mathbf{\Psi}} \hat{\mathbf{\Xi}}) = \hat{\varrho}^2 \|\hat{\mathbf{\Psi}}\|_{\text{dual}}. \quad (55)$$

Since $\hat{\mathbf{\Xi}}$ is Hermitian, its spectral norm satisfies $\varsigma_{\max}(\hat{\mathbf{\Xi}}) \leq \hat{\varrho}^2$, where $\varsigma_{\max}(\cdot)$ denotes the maximum eigenvalue of $\hat{\mathbf{\Xi}}$.

Noting that the nuclear norm is the dual of the spectral norm, the dual norm of $\hat{\mathbf{\Psi}}$ can be written as

$$\|\hat{\mathbf{\Psi}}\|_{\text{dual}} = \|\hat{\mathbf{\Psi}}\|_{\text{nuclear}} = \sum_i \varsigma_i, \quad (56)$$

where $\{\varsigma_i\}$ denote the eigenvalues of $\hat{\mathbf{\Psi}}$.

Furthermore, since $\hat{\mathbf{\Psi}}$ is positive semidefinite and has rank one, its nuclear norm reduces to its trace, i.e., $\|\hat{\mathbf{\Psi}}\|_{\text{dual}} = \text{tr}(\hat{\mathbf{\Psi}})$. Consequently, (55) can be equivalently rewritten as

$$\max_{\|\hat{\mathbf{\Xi}}\| \leq \hat{\varrho}^2} \text{tr}(\hat{\mathbf{\Psi}} \hat{\mathbf{\Xi}}) = \hat{\varrho}^2 \text{tr}(\hat{\mathbf{\Psi}}). \quad (57)$$

This completes the proof.

APPENDIX B

We begin by computing the first-order lower bound of the convex function $\|\hat{\mathbf{t}}_l - \hat{\mathbf{t}}_j\|_2$ at $\hat{\mathbf{t}}_l^{(r)}$, which is given as follows:

$$\|\hat{\mathbf{t}}_l - \hat{\mathbf{t}}_j\|_2 \geq \|\hat{\mathbf{t}}_l^{(r)} - \hat{\mathbf{t}}_j\|_2 + \nabla \left(\|\hat{\mathbf{t}}_l^{(r)} - \hat{\mathbf{t}}_j\|_2 \right)^T \left(\hat{\mathbf{t}}_l - \hat{\mathbf{t}}_l^{(r)} \right), \quad (58)$$

where the gradient term is given by

$$\nabla \left(\|\hat{\mathbf{t}}_l^{(r)} - \hat{\mathbf{t}}_j\|_2 \right) = \frac{\hat{\mathbf{t}}_l^{(r)} - \hat{\mathbf{t}}_j}{\|\hat{\mathbf{t}}_l^{(r)} - \hat{\mathbf{t}}_j\|_2}. \quad (59)$$

Thus, we get

$$\|\hat{\mathbf{t}}_l - \hat{\mathbf{t}}_j\|_2 \geq \|\hat{\mathbf{t}}_l^{(r)} - \hat{\mathbf{t}}_j\|_2 + \frac{1}{\|\hat{\mathbf{t}}_l^{(r)} - \hat{\mathbf{t}}_j\|_2} \left(\hat{\mathbf{t}}_l^{(r)} - \hat{\mathbf{t}}_j \right)^T \left(\hat{\mathbf{t}}_l - \hat{\mathbf{t}}_l^{(r)} \right). \quad (60)$$

Subsequently, we simplify the right-hand side of (60) as follows:

$$\begin{aligned} & \|\hat{\mathbf{t}}_l^{(r)} - \hat{\mathbf{t}}_j\|_2 + \frac{1}{\|\hat{\mathbf{t}}_l^{(r)} - \hat{\mathbf{t}}_j\|_2} \left(\hat{\mathbf{t}}_l^{(r)} - \hat{\mathbf{t}}_j \right)^T \left(\hat{\mathbf{t}}_l - \hat{\mathbf{t}}_l^{(r)} \right) \\ &= \frac{1}{\|\hat{\mathbf{t}}_l^{(r)} - \hat{\mathbf{t}}_j\|_2} \left(\|\hat{\mathbf{t}}_l^{(r)} - \hat{\mathbf{t}}_j\|_2^2 + \left(\hat{\mathbf{t}}_l^{(r)} - \hat{\mathbf{t}}_j \right)^T \left(\hat{\mathbf{t}}_l - \hat{\mathbf{t}}_l^{(r)} \right) \right) \\ &= \frac{1}{\|\hat{\mathbf{t}}_l^{(r)} - \hat{\mathbf{t}}_j\|_2} \left(\left(\hat{\mathbf{t}}_l^{(r)} - \hat{\mathbf{t}}_j \right)^T \left(\hat{\mathbf{t}}_l^{(r)} - \hat{\mathbf{t}}_j \right) \right. \\ & \quad \left. + \left(\hat{\mathbf{t}}_l^{(r)} - \hat{\mathbf{t}}_j \right)^T \left(\hat{\mathbf{t}}_l - \hat{\mathbf{t}}_l^{(r)} \right) \right) \\ &= \frac{1}{\|\hat{\mathbf{t}}_l^{(r)} - \hat{\mathbf{t}}_j\|_2} \left(\hat{\mathbf{t}}_l^{(r)} - \hat{\mathbf{t}}_j \right)^T \left(\left(\hat{\mathbf{t}}_l^{(r)} - \hat{\mathbf{t}}_j \right) + \left(\hat{\mathbf{t}}_l - \hat{\mathbf{t}}_l^{(r)} \right) \right) \\ &= \frac{1}{\|\hat{\mathbf{t}}_l^{(r)} - \hat{\mathbf{t}}_j\|_2} \left(\hat{\mathbf{t}}_l^{(r)} - \hat{\mathbf{t}}_j \right)^T \left(\hat{\mathbf{t}}_l - \hat{\mathbf{t}}_j \right). \end{aligned} \quad (61)$$

Consequently, the following inequality is obtained:

$$\frac{1}{\|\hat{\mathbf{t}}_l^{(r)} - \hat{\mathbf{t}}_j\|_2} \left(\hat{\mathbf{t}}_l^{(r)} - \hat{\mathbf{t}}_j \right)^T \left(\hat{\mathbf{t}}_l - \hat{\mathbf{t}}_j \right) \geq D, \forall l \neq j. \quad (62)$$

This completes the derivation of (46).

REFERENCES

- [1] C.-X. Wang, X. You, X. Gao, X. Zhu, Z. Li, C. Zhang, H. Wang, Y. Huang, Y. Chen, H. Haas *et al.*, "On the road to 6G: Visions, requirements, key technologies, and testbeds," *IEEE Communications Surveys & Tutorials*, vol. 25, no. 2, pp. 905–974, 2023.
- [2] W. Saad, M. Bennis, and M. Chen, "A vision of 6G wireless systems: Applications, trends, technologies, and open research problems," *IEEE network*, vol. 34, no. 3, pp. 134–142, 2019.
- [3] M. Matthaiou, O. Yurduseven, H. Q. Ngo, D. Morales-Jimenez, S. L. Cotton, and V. F. Fusco, "The road to 6G: Ten physical layer challenges for communications engineers," *IEEE Communications Magazine*, vol. 59, no. 1, pp. 64–69, 2021.
- [4] C. Wang, P. Zhang, N. Kumar, L. Liu, and T. Yang, "GCWCN: 6G-based global coverage wireless communication network architecture," *IEEE Network*, vol. 37, no. 3, pp. 218–223, 2022.
- [5] S. Chen, Y.-C. Liang, S. Sun, S. Kang, W. Cheng, and M. Peng, "Vision, requirements, and technology trend of 6G: How to tackle the challenges of system coverage, capacity, user data-rate and movement speed," *IEEE Wireless Communications*, vol. 27, no. 2, pp. 218–228, 2020.
- [6] M. Di Renzo, H. Haas, and P. M. Grant, "Spatial modulation for multiple-antenna wireless systems: A survey," *IEEE Communications Magazine*, vol. 49, no. 12, pp. 182–191, 2011.
- [7] A. F. Molisch, V. V. Ratnam, S. Han, Z. Li, S. L. H. Nguyen, L. Li, and K. Haneda, "Hybrid beamforming for massive MIMO: A survey," *IEEE Communications Magazine*, vol. 55, no. 9, pp. 134–141, 2017.
- [8] L. Zhu, J. Zhang, Z. Xiao, X. Cao, D. O. Wu, and X.-G. Xia, "Millimeter-wave NOMA with user grouping, power allocation and hybrid beamforming," *IEEE Transactions on Wireless Communications*, vol. 18, no. 11, pp. 5065–5079, 2019.
- [9] E. G. Larsson, O. Edfors, F. Tufvesson, and T. L. Marzetta, "Massive MIMO for next generation wireless systems," *IEEE communications magazine*, vol. 52, no. 2, pp. 186–195, 2014.
- [10] C. Ding, J.-B. Wang, H. Zhang, M. Lin, and J. Wang, "Joint MU-MIMO precoding and resource allocation for mobile-edge computing," *IEEE Transactions on Wireless Communications*, vol. 20, no. 3, pp. 1639–1654, 2020.
- [11] L. Zhu, W. Ma, and R. Zhang, "Movable antennas for wireless communication: Opportunities and challenges," *IEEE Communications Magazine*, vol. 62, no. 6, pp. 114–120, 2023.
- [12] —, "Modeling and performance analysis for movable antenna enabled wireless communications," *IEEE Transactions on Wireless Communications*, vol. 23, no. 6, pp. 6234–6250, 2023.
- [13] Z. Xiao, X. Pi, L. Zhu, X.-G. Xia, and R. Zhang, "Multiuser communications with movable-antenna base station: Joint antenna positioning, receive combining, and power control," *IEEE Transactions on Wireless Communications*, 2024.
- [14] L. Zhu, W. Ma, and R. Zhang, "Movable-antenna array enhanced beamforming: Achieving full array gain with null steering," *IEEE Communications Letters*, vol. 27, no. 12, pp. 3340–3344, 2023.
- [15] W. Ma, L. Zhu, and R. Zhang, "MIMO capacity characterization for movable antenna systems," *IEEE Transactions on Wireless Communications*, vol. 23, no. 4, pp. 3392–3407, 2023.
- [16] L. Zhu, W. Ma, Z. Xiao, and R. Zhang, "Performance analysis and optimization for movable antenna aided wideband communications," *IEEE Transactions on Wireless Communications*, 2024.
- [17] Y. Mao, O. Dizdar, B. Clerckx, R. Schober, P. Popovski, and H. V. Poor, "Rate-splitting multiple access: Fundamentals, survey, and future research trends," *IEEE communications surveys & tutorials*, vol. 24, no. 4, pp. 2073–2126, 2022.
- [18] B. Clerckx, Y. Mao, E. A. Jorswieck, J. Yuan, D. J. Love, E. Erkip, and D. Niyato, "A primer on rate-splitting multiple access: Tutorial, myths, and frequently asked questions," *IEEE Journal on Selected Areas in Communications*, vol. 41, no. 5, pp. 1265–1308, 2023.
- [19] M. R. Camana, C. E. Garcia, and I. Koo, "Rate-splitting multiple access in a MISO SWIPT system assisted by an intelligent reflecting surface," *IEEE Transactions on Green Communications and Networking*, vol. 6, no. 4, pp. 2084–2099, 2022.
- [20] Y. Liu, X. Liu, X. Mu, T. Hou, J. Xu, M. Di Renzo, and N. Al-Dhahir, "Reconfigurable intelligent surfaces: Principles and opportunities," *IEEE communications surveys & tutorials*, vol. 23, no. 3, pp. 1546–1577, 2021.
- [21] M. Asif, X. Bao, A. Ihsan, W. U. Khan, M. Ahmed, and X. Li, "Securing noma 6g communications leveraging intelligent omni-surfaces under residual hardware impairments," *IEEE Internet of Things Journal*, vol. 11, no. 14, pp. 25 326–25 336, 2024.
- [22] A. Ihsan, W. Chen, M. Asif, W. U. Khan, Q. Wu, and J. Li, "Energy-efficient IRS-aided NOMA beamforming for 6G wireless communications," *IEEE Transactions on Green Communications and Networking*, vol. 6, no. 4, pp. 1945–1956, 2022.
- [23] M. Asif, X. Bao, A. Ihsan, W. U. Khan, X. Li, S. Chatzinotas, and O. A. Dobre, "Noma-based ze-ris empowered backscatter communication with energy-efficient resource management," *IEEE Transactions on Communications*, 2025.
- [24] A. Amhaz, S. Khisa, M. Elhattab, C. Assi, and S. Sharafeddine, "Enhancing comp-rsma performance with movable antennas: A meta-learning optimization framework," *IEEE Transactions on Communications*, 2026.
- [25] X. Li, Z. Du, Q. Cui, Y. Hou, J. Zhang, and X. Tao, "Movable Antennas-Enhanced RSMA Short-Packet Transmission for URLLC Services," *IEEE Internet of Things Journal*, 2025.
- [26] B. Fang, X. Li, Z. Zhu, Q. Cui, C. Gao, and X. Tao, "Toward Spectral-Efficient URLLC: A Novel Movable Antenna-Aided Uplink RSMA Design for mBRLC Services," *IEEE Wireless Communications Letters*, vol. 15, pp. 1360–1364, 2026.
- [27] H. Wu, H. Ren, C. Pan, and Y. Zhang, "Movable antenna-enabled RIS-aided integrated sensing and communication," *IEEE Transactions on Cognitive Communications and Networking*, 2025.
- [28] Y. Ma, K. Liu, Y. Liu, L. Zhu, and Z. Xiao, "Movable-antenna aided secure transmission for RIS-ISAC systems," *IEEE Transactions on Wireless Communications*, 2025.
- [29] Y. Sun, H. Xu, B. Ning, Z. Cheng, C. Ouyang, and H. Yang, "Sum-rate optimization for RIS-aided multiuser communications with movable antennas," *IEEE Wireless Communications Letters*, 2024.
- [30] W. Xie, Z. Li, C. Yu, H. Xu, J. Wang, W. Wu, X. Li, and L. Yang, "Movable antenna-assisted covert communications with reconfigurable intelligent surfaces," *IEEE Internet of Things Journal*, 2024.
- [31] Y. Sun, H. Xu, B. Ning, L. Zhu, C. Ouyang, and H. Yang, "STAR-RIS aided communication system with movable antennas exploiting statistical CSI," *IEEE Communications Letters*, 2025.
- [32] M. Hu, N. Liu, and W. Kang, "Sum Rate optimization for RIS-Aided RSMA system with Movable Antenna," *arXiv preprint arXiv:2512.23242*, 2025.
- [33] Q. Zhang, J. Liu, Z. Gao, Z. Li, Z. Peng, Z. Dong, and H. Xu, "Robust beamforming design for RIS-aided NOMA secure networks with transceiver hardware impairments," *IEEE Transactions on Communications*, vol. 71, no. 6, pp. 3637–3649, 2023.
- [34] Z. Li, W. Chen, Q. Wu, H. Cao, K. Wang, and J. Li, "Robust beamforming design and time allocation for IRS-assisted wireless powered communication networks," *IEEE Transactions on Communications*, vol. 70, no. 4, pp. 2838–2852, 2022.
- [35] S. Boyd, L. El Ghaoui, E. Feron, and V. Balakrishnan, *Linear matrix inequalities in system and control theory*. SIAM, 1994.
- [36] W. Ni, X. Liu, Y. Liu, H. Tian, and Y. Chen, "Resource allocation for multi-cell IRS-aided NOMA networks," *IEEE Transactions on Wireless Communications*, vol. 20, no. 7, pp. 4253–4268, 2021.
- [37] S. J. Wright, *Primal-dual interior-point methods*. SIAM, 1997.
- [38] Y. Zheng, S. A. Tegos, Y. Xiao, P. D. Diamantoulakis, Z. Ma, and G. K. Karagiannidis, "Zero-energy device networks with wireless-powered RISs," *IEEE Transactions on Vehicular Technology*, vol. 72, no. 10, pp. 13 655–13 660, 2023.